



Modeling the mechanism of micro/nanostructured surface formation in Al-Co-Cr-Fe-Ni and Co-Cr-Fe-Mn-Ni high-entropy alloys treated with a high current pulsed electron beam

S. A. Nevskii¹, V. D. Sarychev¹, S. V. Konovalov^{†,1,2}, K. A. Osintsev^{1,2}, Yu. F. Ivanov^{1,3},

I. A. Panchenko¹, V. E. Gromov¹

[†]konovalov@sibsiu.ru

¹Siberian State Industrial University, Novokuznetsk, 654007, Russia

²Samara National Research University, Samara, 443086, Russia

³Institute of High Current Electronics SB RAS, Tomsk, 634055, Russia

In this work, we investigated, using transmission and scanning electron microscopy, the microstructure of Al-Co-Cr-Fe-Ni and Co-Cr-Fe-Mn-Ni non-equimolar high-entropy alloys treated by high current pulsed electron beams with an energy density of 30 J/cm². Both alloys revealed a cellular crystallization structure with an average cell size of 192 ± 5 nm, and 453 ± 6 nm, correspondingly. The study aims to improve the model of the mechanism of formation of micro- and nanostructured surface layers taking into account combined thermocapillary, concentration-capillary, evaporative-capillary and thermoelectric instabilities at the melt-plasma interface. The results of the linear stability analysis showed that the absorbed power density is lost by evaporation that leads to a decrease in the values of the gradient of the undisturbed temperature and, an increase in the wavelength at which the maximum rate of growth of disturbances is observed. An analysis of the dispersion equation showed that the values of the wavelengths of disturbances on the surface of alloys in the liquid phase are 454 nm for Co-Cr-Fe-Mn-Ni and 189 nm for Al-Co-Cr-Fe-Ni, which deviate from the experimental data by no more than 2%.

Keywords: high-entropy alloys, high current pulsed electron beam treatment, thermocapillary instability, thermoelectric effect, concentration-capillary effect.

1. Introduction

High-entropy alloys (HEAs) are a relatively new class of multicomponent materials, which mainly contain more than five principal elements varying from 5 to 35 at.%. Such a chemical composition increases the configurational entropy of the thermodynamic system comparing to pure metals or conventional alloys and leads to the formation of a unique microstructure and properties. Due to the high entropy of mixing and other effects such as sluggish diffusion and severe distortion of a crystal lattice, this type of alloys shows good balance between strength and ductility, high hardness, good wear, and corrosion resistance, as well as excellent performance at cryogenic temperatures. These properties make HEAs attractive for many industrial applications.

Al-Co-Cr-Fe-Ni and Co-Cr-Fe-Mn-Ni systems appeared among the first high-entropy alloys, and are currently being widely investigated. Previous studies demonstrated that the chemical composition and routes of their formation strongly influence the microstructure and subsequent physical and mechanical behavior [1]. There are various methods of fabrication of bulk HEAs: vacuum arc melting [2], vacuum induction melting [3], selective laser melting [4] and

additive manufacturing methods such as wire-arc additive manufacturing [5] and laser cladding [6].

The methods of surface modification also play an important role in the design of HEAs since they allow eliminating some defects as pores or microcracks and increasing durability. For example, the HEA surface can be modified by plasma nitriding [7], laser remelting [8], boronizing [9], gaseous carburization [10], ultrasonic nanocrystal surface modification [11] and high current pulsed electron beam treatment (HCPEB) [12,13]. The latter method introduces high energies into the surface layers and forms a cellular microstructure with a grain size of 100 – 500 nm, leading to better mechanical and tribological characteristics.

The mechanism for the formation of such a structure with very fine rounded grains is still under development. In our previous article, we made an approach to the model of this mechanism considering the contribution of thermocapillary and thermoelectric instability arising on the molten surface [14]. We assumed that the reason for the formation of a cellular structure is a combination of thermal, evaporation-capillary, and thermoelectric instabilities, since they become important at temperature gradients of 10⁶ K/m and molten layer thicknesses of ~1–100 μm [6,7]. According to the

results of [12,13], with an increase in the number of pulses or the energy density of the electron beam (E_s), the size of the crystallization cells increases. From the hydrodynamic point of view [14], this can be explained by the fact that with increasing E_s values, the losses of the power density of the absorbed electron beam for evaporation increase. This, in turn, leads to a decrease in the gradient of the undisturbed temperature and a shift in the wavelength values to the submicroscopic range, which accounts for the maximum rate of growth of perturbations of the melt surface. The model proposed in [14] does not provide an adequate explanation for these facts, since it does not take into account concentration-capillary effects and losses of absorbed power density for evaporation. Therefore, the aim of this study is to improve the model of cellular microstructure formation in high-entropy alloys of Al-Co-Cr-Fe-Ni and Co-Cr-Fe-Mn-Ni systems treated with high-current electron beams [14] taking into account these effects.

2. Materials and methods

Al-Co-Cr-Fe-Ni and Co-Cr-Fe-Mn-Ni HEAs were fabricated by wire-arc additive manufacturing using cable-type welding wires as feeding materials and Ar as a shielding gas (99.99% purity) [13]. Al-Co-Cr-Fe-Ni welding wire with a diameter of 1.2 mm was composed of Al wire (Al, 99.9 at.%, \varnothing 0.5 mm), Cr-Ni wire (Cr, 20 at.%, Ni, 80 at.%, \varnothing 0.4 mm), and Co-Fe-Ni wire (Co, 17 at.%, Fe, 54 at.%, Ni, 29 at.%, \varnothing 0.4 mm). The samples were deposited on a steel substrate (C 0.209%, Si 0.273%, Mn 0.483%, Fe — balanced) with the following process parameters: wire feed speed 8 m/min, voltage 17 V, travel speed 0.3 m/min, substrate heating temperature $\approx 250^\circ\text{C}$.

Co-Cr-Fe-Mn-Ni welding wire with a diameter of 1 mm was composed of Co wire (Co, 99.9 at.%, \varnothing 0.5 mm); Autrod 16.95 wire (Fe, 65 at.%, Cr, 20 at.%, Ni, 7 at.%, Si, 2 at.%, Mn, 6 at.%, \varnothing 0.7 mm), and Cr-Ni wire (Cr, 20 at.%, Ni, 80 at.%, \varnothing 0.4 mm). The samples were deposited on a 321 stainless steel substrate with the following process parameters: wire feed speed 13 m/min, travel speed 0.1 m/min, and welding voltage 22 V.

The chemical composition of the Co-Cr-Fe-Mn-Ni after deposition was Co 28 at.%, Cr 15.0 at.%, Fe 37 at.%, Mn 5 at.%, Ni 15 at.%, and of the Al-Co-Cr-Fe-Ni — Al 36 at.%, Co 5 at.%, Cr 8 at.%, Fe 17 at.%, Ni 34 at.%.

Both fabricated alloys were irradiated by a high current pulsed electron beam using a “SOLO” unit (Institute of High Current Electronics, Tomsk, Russia) [15]. The treatment mode was the following: the energy of accelerated electrons 18 keV, the energy density of an electron beam 30 J/cm², the duration of a beam pulse 50 μs , the pulse frequency 0.3 s⁻¹, a number of pulses 3, residual pressure of an inert gas (Ar) in the processing chamber $2 \cdot 10^{-2}$ Pa.

The surface of the alloys after treatment was analyzed using a scanning electron microscope (SEM) (LEO EVO 50, ZEISS, Oberkochen, Germany) and a transmission electron microscope (TEM) JEM-2100 instrument, JEOL, Tokyo, Japan). The foil for TEM was prepared by ion etching (an EM-09100IS ion slicer unit from JEOL, Tokyo, Japan) in an Ar atmosphere. An intercept technique was implemented to determine the average grain sizes.

3. Linear stability analysis

Previous studies showed that the size of cellular grains has a direct correlation with the value of energy density of a high current electron beam: the higher the energy density, the larger the grain size [14]. This can be interpreted by the occurrence of the combined thermal, concentration-capillary, thermoelectric instabilities as well as the crystallization front instability.

In this study, we consider the combined instability on the surface of the melted layer with the thickness h . Currently, the theory of surface tension of molten HEAs systems and the experimental data on the temperature dependence of their surface tension are not available in the literature. Hence, we suggest to study the effect of the concentration of alloying elements by modeling HEAs as CoCrFeNi-Al and CrMnCoNi-Fe systems. For this, we used linearized equations of Navier-Stokes, convective thermal conductivity, and the liquid phase diffusion [16]:

$$\begin{aligned} \frac{\partial u}{\partial t} &= -\frac{1}{\rho} \nabla p + \nu \Delta u, \\ \frac{\partial w}{\partial t} &= -\frac{1}{\rho} \nabla p + \nu \Delta w, \quad \frac{\partial u}{\partial x} + \frac{\partial w}{\partial z} = 0, \\ \frac{\partial T_1}{\partial t} + wG_0 &= \chi \left(\frac{\partial^2 T_1}{\partial x^2} + \frac{\partial^2 T_1}{\partial z^2} \right), \\ \frac{\partial C_1}{\partial t} + wG_1 &= D \left(\frac{\partial^2 C_1}{\partial x^2} + \frac{\partial^2 C_1}{\partial z^2} \right), \end{aligned} \tag{1}$$

where T_1 — the temperature disturbance of the liquid phase, u , w — the components of the disturbance vector of the molten flow velocity, p — the pressure disturbance, C_i — the disturbance of the alloying element concentration, χ — the thermal diffusivity of the liquid material, D — the diffusivity coefficient of the alloying element in the molten, ν — the kinematic viscosity of the molten, ρ — the density of the molten surface layer, G_0 — the gradient of the undisturbed temperature, G_1 — the gradient of the undisturbed concentration.

The system of Eqs. (1) must be completed with boundary conditions. At the boundary of the molten surface $z=0$, the condition for the equality of normal and tangential stresses is as follows:

$$\begin{aligned} \rho \nu \left(\frac{\partial u}{\partial z} + \frac{\partial w}{\partial x} \right) &= \frac{\partial \gamma}{\partial x} - \tau_{xz}^{el}; \\ -(p + p_e) + 2\rho \nu \frac{\partial w}{\partial z} &= \gamma_m \frac{\partial^2 \eta}{\partial x^2}, \end{aligned} \tag{2}$$

where $\gamma = \gamma_m + \sigma_T(T_1 + G_0\eta) + \sigma_c(C_1 + G_1\eta)$ — the surface tension, γ_m — the surface tension under the melting temperature, η — the deviation of the molten surface from its undisturbed position, p_e — the electrical field contribution into pressure, τ_{xz}^{el} — the tangent component of Maxwell stress tensor. According to [16,17] the contribution of the electric field into pressure is as follows: $p_e = \varepsilon \varepsilon_0 k E_0^2 \eta$, E_0 — the undisturbed value of the electric field intensity, where ε — the permittivity, ε_0 — the permittivity of vacuum. Respectively, the tangent component of Maxwell stress tensor

is — $\tau_{xz}^{el} = -\varepsilon\varepsilon_0 E_0^2 \frac{\partial \eta}{\partial x}$. Taking this into account conditions (2) are as follows:

$$\begin{aligned} \rho v \left(\frac{\partial u}{\partial z} + \frac{\partial w}{\partial x} \right) &= \sigma_T \left(\frac{\partial T_l}{\partial x} + G_0 \frac{\partial \eta}{\partial x} \right) + \\ &+ \sigma_C \left(\frac{\partial C_l}{\partial x} + G_1 \frac{\partial \eta}{\partial x} \right) + \varepsilon\varepsilon_0 E_0^2 \frac{\partial \eta}{\partial x}, \\ -(p + \varepsilon\varepsilon_0 k E_0^2 \eta) + 2\rho v \frac{\partial w}{\partial z} &= \gamma_m \frac{\partial^2 \eta}{\partial x^2}. \end{aligned} \quad (3)$$

The kinematic boundary conditions and the conditions for the thermal conductivity and diffusion equations are as follows:

$$z = 0 : w = \frac{\partial \eta}{\partial t}, \frac{\partial T_l}{\partial z} = 0; z = -h : u = 0, w = 0, T = 0. \quad (4)$$

In contrast to [17], we take into account the influence of molten boundary deformation upon temperature and concentration disturbances. Like the authors in [14,17], we suppose that the disturbance range of the boundary surface is $\eta_0 \ll h$, then $z \rightarrow -\infty$. The system of (1), (3), (4) is solved as follows:

$$\begin{aligned} u(x, z, t) &= -\frac{i}{k} (A_1 k \exp(kz) + A_2 k_1 \exp(k_1 z)) \exp(\omega t - ikx), \\ w(x, z, t) &= (A_1 \exp(kz) + A_2 \exp(k_1 z)) \exp(\omega t - ikx), \\ p(x, z, t) &= \frac{\rho v}{k} (k^2 - k_1^2) \exp(kz) \exp(\omega t - ikx), \\ T(z) &= \frac{G_0}{\omega} ((A_1 k - A_2 k_1 \delta) \exp(k_2 z) + A_2 \delta \exp(k_1 z) - \\ &- A_1 \exp(kz)) \exp(\omega t - ikx), \end{aligned} \quad (5)$$

$$\begin{aligned} C(z) &= \frac{G_1}{\omega} ((A_1 k - A_2 k_1 \delta) \exp(k_3 z) + A_2 \delta_1 \exp(k_1 z) - \\ &- A_1 \exp(kz)) \exp(\omega t - ikx), \\ \eta &= \eta_0 \exp(\omega t - ikx), \end{aligned}$$

where $k_1 = \sqrt{k^2 + (\omega/v)}$, $k_2 = \sqrt{k^2 + (\omega/\chi)}$, $k_3 = \sqrt{k^2 + (\omega/D)}$, $\omega = \alpha + i\Omega$, α — the growth rate of the boundary surface disturbances, Ω — the cyclic frequency. Using (5) in (3) and (4), we arrive at the following system of equations for the constants A_1 and A_2 :

$$\begin{aligned} \left(1 + \frac{k_1^2}{k^2} + \frac{\omega_c^2}{\omega\omega_v} + \frac{\omega_p}{\omega} \left(\frac{k}{k_2} - 1 \right) \right) A_1 + \\ + \left(\frac{2k_1}{k} + \left(1 - \frac{k_1}{k_2} \right) \frac{\delta\omega_p}{\omega} + \frac{\omega_c^2}{\omega\omega_v} \right) A_2 = 0, \\ \left(2 - \frac{k}{\omega} \left(\frac{\omega_T}{k_2} + \frac{\omega_C}{k_3} \right) + \frac{\omega_E}{\omega} \right) A_1 + \\ + \left(1 + \frac{k_1^2}{k^2} + \frac{\omega_T}{\omega} \left(\left(\frac{k_1}{k_2} - 1 \right) \delta - 1 \right) \right) + \\ + \frac{\omega_C}{\omega} \left(\left(\frac{k_1}{k_3} - 1 \right) \delta_1 - 1 \right) + \frac{\omega_E}{\omega} \right) A_2 = 0, \end{aligned} \quad (6)$$

where $\omega_T = \sigma_T G_0 / (\rho v)$, $\omega_C = \sigma_C G_1 / (\rho v)$, $\omega_v = vk^2$, $\omega_c^2 = \gamma_m k^3 / \rho - \varepsilon\varepsilon_0 E_0^2 k^2 / \rho$, $\omega_p = p'_v G_0 / (\rho vk)$, $\omega_E = \varepsilon\varepsilon_0 E^2 / (\rho v)$, $\delta = \text{Pr} / (1 - \text{Pr})$, $\delta_1 = \text{Sc} / (1 - \text{Sc})$, $\text{Pr} = v/\chi$ — Prandtl number,

$\text{Sc} = v/D$ — Schmidt number. The nontrivial solution of system (6) requires its determinant being equal zero, the determinant, in its turn being a dispersion equation:

$$\begin{aligned} R_T - R_C - R_E - R_V - R_\sigma &= 0, \\ R_\sigma &= \omega^2 \left((\omega + 2\omega_v)^2 + \omega_c^2 \right) - \frac{4\omega^2 \omega_v^2 k_1}{k}, \\ R_T &= \omega_T \omega_v \left(\left(\delta \left(1 - \frac{k_1}{k_2} \right) + \left(1 - \frac{k}{k_2} \right) \right) \omega_v \omega_p + \right. \\ &+ \left(-\delta\omega_c^2 - 2\omega_v \omega (\delta + 1) - \delta\omega^2 \right) \left(1 - \frac{k_1}{k_2} \right) - \\ &\left. - \omega_c^2 \left(1 - \frac{k}{k_2} \right) - \omega^2 \right), \\ R_C &= \omega_T \omega_v \left(\left(\delta \left(1 - \frac{k_1}{k_2} \right) \frac{k}{k_3} + \left(\delta_1 \left(1 - \frac{k_1}{k_3} \right) + 1 \right) \left(1 - \frac{k}{k_2} \right) \right) \omega_v \omega_p + \right. \\ &+ \left(-\delta_1 \omega_c^2 - 2\omega_v \omega (\delta_1 + 1) - \delta\omega^2 \right) \left(1 - \frac{k_1}{k_3} \right) - \\ &\left. - \omega_c^2 \left(1 - \frac{k}{k_3} \right) - \omega^2 \right), \\ R_E &= -\omega_E \omega_v \omega \left(\left(1 - \frac{k_1}{k} \right) \omega_v + \omega \right), \\ R_V &= \omega_p \omega_v \left(\left(\delta \left(1 - \frac{k_1}{k_2} \right) + \left(1 - \frac{k}{k_2} \right) \right) \omega_E \omega_v + \right. \\ &\left. + 2\delta\omega\omega_v \left(1 - \frac{k_1}{k_2} \right) + (2\omega_v + \omega) \omega \left(1 - \frac{k}{k_2} \right) \right). \end{aligned} \quad (7)$$

In liquid metals Prandtl and Schmidt numbers possess values $\text{Pr} \ll 1$ and $\text{Sc} \ll 1$, then dispersion Eq. (7) with consideration to replacing $z = k_1/k$ and $\omega = \omega_v(z^2 - 1)$ will be as follows:

$$\begin{aligned} ((-C^2 + 2C_4 + 2(z^2 - 1)(z + 1))\text{Pr} - 2(z^2 - 1))C_2 + \\ + (2C_4 \text{Pr} - C^2 \text{Sc} + 2(z^2 - 1)(z + 1)\text{Sc} - 2(z^2 - 1))C_3 - \\ - (2C_5 + (z^2 - 1)(z^2 + 2z + 3))\text{Pr}C_4 - 2(z^2 - 1)C_5 + \\ + (z + 1)^2 (C^2 + (z^2 + 1)^2 - 4z) = 0, \end{aligned} \quad (8)$$

where $C = \omega_c/\omega_v$, $C_2 = \omega_T/(2\omega_v)$, $C_3 = \omega_C/(2\omega_v)$, $C_4 = \omega_p/(2\omega_v)$, $C_5 = \omega_E/(2\omega_v)$. Let us take $\text{Re}(z) > 0$ and $\text{Re}(\omega) > 0$ as a criterion for the instability of disturbances. If it is fulfilled, the disturbances will increase without a limit at a rate of $\alpha = \alpha(\lambda)$. The wavelength λ_m , under which the maximum of this dependence is observed, will determine the size of the formed crystallization cells. Let us calculate the temperature gradient as: $G_0 = q/k(1 - q_{\text{out}}/q)$ where $q = E_s/t_0$ — the power density of the electron beam, E_s — energy per unit area of the electron beam, q_{out} — power per unit area determined by the evaporation process, k — the thermal conductivity of the liquid metal, $q_{\text{out}}/q < 1$ — the loss of power density by evaporation. Table S1 (Supplementary material) provides the data for the numerical solution of Eq. (8). The value of the thermoelectrical coefficient γ is chosen within the range from 0.1 to 4 V/K [14,17]. The choice of such values for this coefficient is determined by the fact that the convective current intensifies the thermoelectric effects in the liquid metal. The values of viscosity and surface tension, as well as

those of the thermal diffusivity, at first approximation will be calculated according to the mixture rule: $X = \sum_{i=1}^5 a_i x_i$, where a_i — part per volume of the i -th component of the alloy, x_i — the viscosity (thermal diffusivity, surface tension) of the i -th component of the alloy.

4. Results and discussion

Treatment with a high current pulsed electron beam at an energy density of 30 J/cm² forms cellular surface structures in Co-Cr-Fe-Mn-Ni and Al-Co-Cr-Fe-Ni alloys (Fig. 1). The cell size in the first alloy is 2.3 times larger than in the second.

For modeling the mechanism of formation of surface structures in the first case, we assume that the influence of the thermoelectric effects (C_5) upon the tangential stresses and the evaporation pressure (C_4) upon the normal stresses at the molten boundary equals to zero, which is equivalent to $C_4=0$ and $C_5=0$. The influence of thermoelectric effects is taken into account only for the frequency of the capillary wave. So, we can estimate the initial wavelength as the following:

$$\omega = -2\omega_v - \frac{\omega_r Pr}{4} - \frac{\omega_c Sc}{4} \pm i\omega_c. \quad (9)$$

Then the contribution of the thermoelectric field is decisive if ω_c takes on complex values, which is satisfied under the condition $E_0^2 > 2\pi\gamma_m / (\epsilon\epsilon_0\lambda)$. For Al-Co-Cr-Fe-Ni alloy the instability of the disturbance wavelengths in the nano range occurs under $E_0 > 3.32 \cdot 10^7$ V/m, and for Co-Cr-Fe-Mn-Ni alloy under $E_0 > 3.5 \cdot 10^7$ V/m.

Figure 2 provides the dependence between the values of $\alpha = \alpha(\lambda)$ and the values of the field intensity under various

values of q_{out}/q . The q corresponds to the energy density of the electron beam of 30 J/cm². As the losses by evaporation grow, the value of the temperature gradient decreases and the value of disturbance wavelength λ_m associated with the maximum of $\alpha = \alpha(\lambda)$ grows. This is due to a slower change in surface tension compared to the case of the absence of these losses and, as a consequence, a lower value of tangential stresses at the melt boundary [21]. As a result, instability occurs in the region of larger wavelengths.

In the first case (Fig. 2) for the Co-Cr-Fe-Mn-Ni system the value of $\lambda_m = 430$ nm is the closest to the size of cells d obtained experimentally ($d = 453 \pm 6$ nm (Fig. 1c)). It was observed at $q_{out}/q = 0.4$ and the thermoelectric coefficient, $\gamma = 0.31$ V/K. For the Al-Co-Cr-Fe-Ni system the value of $\lambda_m = 186$ nm was obtained at $q_{out}/q = 0.3$, $\gamma = 2.31$ V/K ($d = 192 \pm 5$ nm (Fig. 1d)).

In the second case, we take into account the contribution of thermoelectric effects upon the tangential stresses ($C_4 = 0$, $C_5 \neq 0$) that leads to growing of the disturbance wavelength λ_m to 454 nm for Co-Cr-Fe-Mn-Ni alloy and to 189 nm for Al-Co-Cr-Fe-Ni (Fig. 3).

In the third case we take into account the evaporation pressure of $\sim 10^9$ Pa ($C_4 \neq 0$, $C_5 = 0$) that demonstrates no effects on the value of λ_m for Al-Co-Cr-Fe-Ni which remains stable (189 nm). However, the value of λ_m for Co-Cr-Fe-Mn-Ni increases to 477 nm (Fig. 4). We suggest that the reason for this is the difference in the chemical compositions of the alloys. The further investigation should be carried out to test this hypothesis.

The results obtained in this study show that various thermocapillary, concentration-capillary and thermoelectric

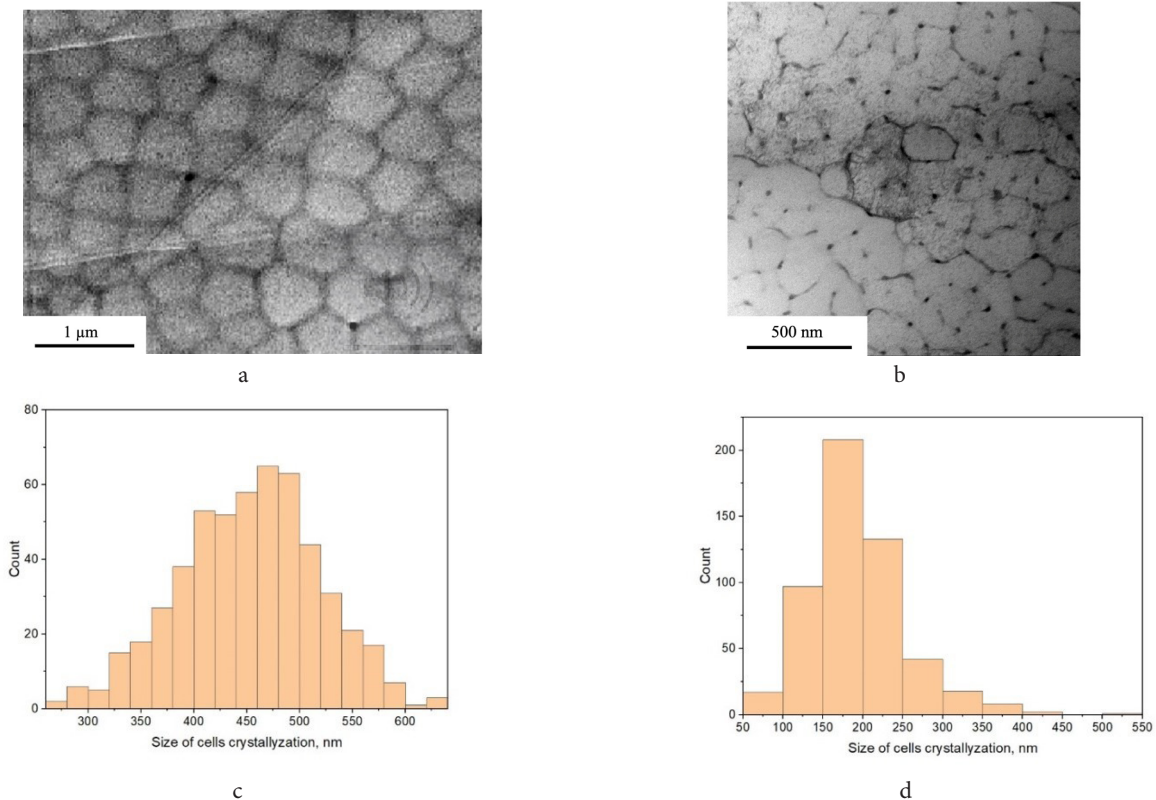


Fig. 1. SEM-micrograph of Cr-Mn-Fe-Co-Ni HEA (a) and TEM micrograph of Al-Co-Cr-Fe-Ni after treatment with a high current pulsed electron beam at an energy density of the electron beam of 30 J/cm² (b), histogram to Fig. 1a (c), histogram to Fig. 1b (d).

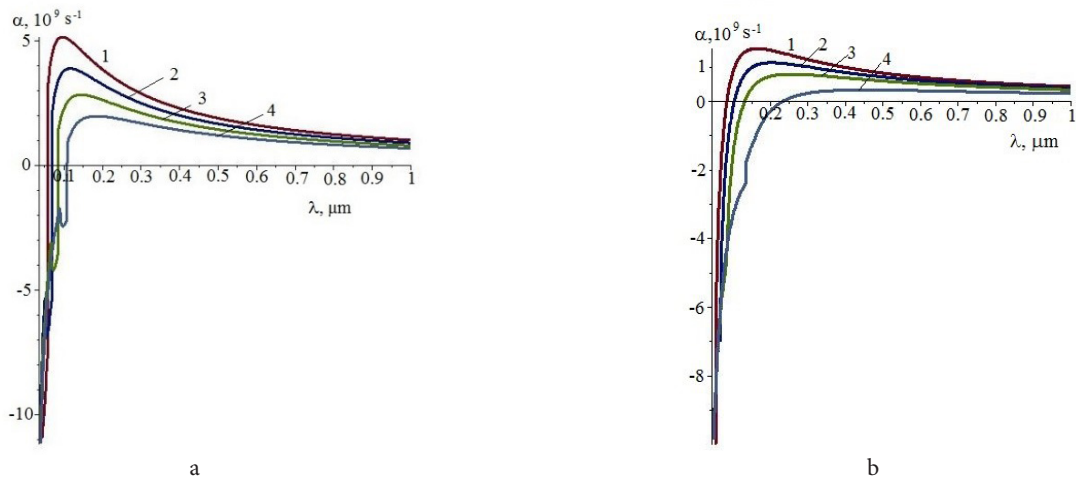


Fig. 2. (Color online) The dependences between the growth rate of the molten surface disturbances and the disturbance wavelength for (a) Al-Co-Cr-Fe-Ni and (b) Co-Cr-Fe-Mn-Ni treated by HCPEB with the energy density of 30 J/cm^2 . Numbers indicate various values of power density losses by evaporation q_{out}/q (1–0.1; 2–0.2; 3–0.3; 4–0.4).

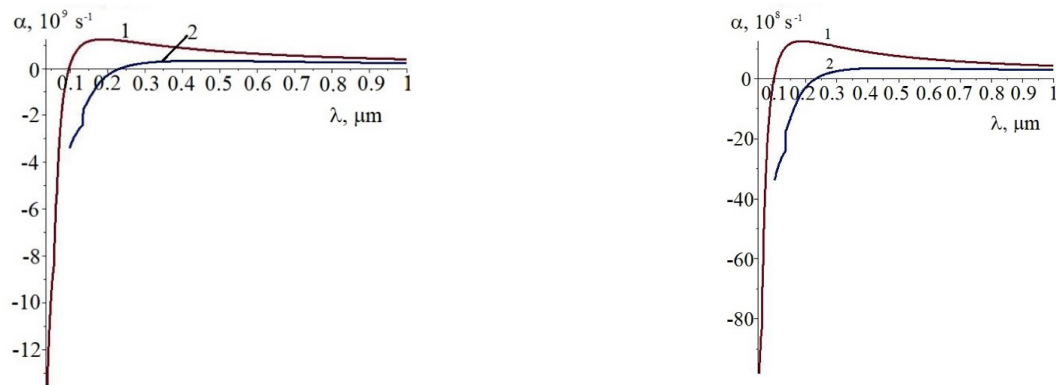


Fig. 3. (Color online) The dependences between the growth rate of the molten surface disturbances and the disturbance wavelength for 1 — Al-Co-Cr-Fe-Ni; 2 — Co-Cr-Fe-Mn-Ni. The thermoelectric field under the boundary conditions for the tangential stresses was taken into account.

Fig. 4. (Color online) The dependences between the growth rate of the molten surface disturbances and the disturbance wavelength for 1 — Al-Co-Cr-Fe-Ni; 2 — Co-Cr-Fe-Mn-Ni. The evaporation pressure of 10^9 Pa was taken into account.

instabilities should be taken into account to properly calculate the disturbance wavelength and consequently determine the size of the cells in the surface of HEAs treated by high current pulsed electron beams. The relative error of the calculated results, determined as $\delta = (\lambda_m - d) d \cdot 100\%$, where d is an average size of cells, showed that the closest values were obtained when the contribution of thermoelectric effects upon the tangential stresses was taken into account. In this case the relative error is not more than 2%.

5. Conclusions

In this study, we proposed a model of the mechanism of formation of micro- and nanostructured surfaces in high-entropy alloys of the Al-Co-Cr-Fe-Ni and Co-Cr-Fe-Mn-Ni systems treated with high current pulsed electron beams with an energy density of 30 J/cm^2 . The main conclusions could be drawn:

1. High-current pulsed electron beam treatment of the Al-Co-Cr-Fe-Ni and Co-Cr-Fe-Mn-Ni systems leads to the formation of micro- and nanostructured surfaces with cellular grains. Co-Cr-Fe-Mn-Ni system has cell sizes of $453 \pm 6 \text{ nm}$, and the Al-Co-Cr-Fe-Ni alloy — $192 \pm 5 \text{ nm}$.

2. The contribution of evaporation should be taken into account because it may lead to a decrease in the gradient of the undisturbed temperature, a decrease in the strength of the thermoelectric field in the melt, a slower change in the surface tension and, as a consequence, an increase in the wavelength, which accounts for the maximum rate of growth of disturbances of the melt surface. The vapor recoil pressure for the Al-Co-Cr-Fe-Ni alloy does not lead to a significant change in λ_m , whereas for Co-Cr-Fe-Mn-Ni it increases.

3. The dependences of the growth rate of the molten surface disturbances upon the wavelength showed one maximum. For Co-Cr-Fe-Mn-Ni the maximum is observed under the value of 454 nm , and for Al-Co-Cr-Fe-Ni alloy — 189 nm .

4. The calculation results demonstrated a correlation with the experimental data with a relative error of no more than 2%.

Supplementary material. The online version of this paper contains supplementary material available free of charge at the journal's Web site (lettersonmaterials.com).

Acknowledgements. The work is performed under the financial support of Russian Science Foundation [#20-19-00452].

References

1. J.-W. Yeh. JOM. 65, 1759 (2013). [Crossref](#)
2. Y.P. Wang, B.S. Li, M.X. Ren, C. Yang, H.Z. Fu. Mat. Sci. and Eng.: A. 491, 154 (2008). [Crossref](#)
3. N. Choi, N. Park, J. Kim, A.V. Karasev, P.G. Jönsson, J.H. Park. Metals. 10 (10), 1286 (2020). [Crossref](#)
4. D. Karlsson, A. Marshal, F. Johansson, M. Schuisky, M. Sahlberg, J.M. Schneider, U. Jansson. J. of All. and Comp. 784, 195 (2019). [Crossref](#)
5. K. A. Osintsev, S. V. Konovalov, A. M. Glezer, V. E. Gromov, Yu. F. Ivanov, I. A. Panchenko, R. V. Sundeev. Mat. Letters. 294, 129717 (2021). [Crossref](#)
6. W. Guo, N. Ding, G. Liu, C. Jing, H. Xu, L. Liu, N. Xu, X. Wu, J. He, F. Zairi. Mat. Character. 184, 111660 (2022). [Crossref](#)
7. J. Hou, W. Song, L. Lan, J. Qiao. J. of Mat. Sci. and Tech. 48, 140 (2020). [Crossref](#)
8. T.M. Yue, H. Xie, X. Lin, H. Yang, G. Meng. Entropy. 15 (7), 2833 (2013). [Crossref](#)
9. H. Nakajo, A. Nishimoto. Journal of Manufacturing and Materials Processing. 6 (2), 29 (2022). [Crossref](#)
10. Y. Peng, J. Gong, T.L. Christiansen, M.A. J. Somers. Materials Letters. 283, 128896 (2021). [Crossref](#)
11. T. A. Listyawan, H. Lee, N. Park. J. of Mat. Sci. and Tech. 59, 37 (2020). [Crossref](#)
12. P. Lyu, Y. Chen, Z. Liu, J. Cai, C. Zhang, Y. Jin, Q. Guan, N. Zhao. Appl. Surf. Sci. 504, 144453 (2020). [Crossref](#)
13. K. Osintsev, V. Gromov, Y. Ivanov, S. Konovalov, I. Panchenko, S. Vorobyev. Metals. 11 (8), 1228 (2021). [Crossref](#)
14. S. Nevskii, S. Konovalov, K. Osintsev, Yu. Ivanov, A. Y. Granovskii, V. Gromov. Letters on Materials. 11 (3), 309 (2021). [Crossref](#)
15. D. I. Proskurovsky, V. P. Rotshtein, G. E. Ozur, Yu. F. Ivanov, A. B. Markov. Surface and Coatings Technology. 125, 49 (2000). [Crossref](#)
16. S. Nevskii, V. Sarychev, S. Konovalov, A. Granovskii, V. Gromov. Metals. 10 (10), 1399 (2020). [Crossref](#)
17. S.A. Astapchik, N.A. Bereza. Phys. Metals and Metallography. 103, 1 (2007). [Crossref](#)
18. S. Uporov, V. Bykov, S. Pryanichnikov, A. Shubin, N. Uporova. Intermetallics. 83, 1 (2019). [Crossref](#)
19. S. Rohila, R.B. Mane, G. Ummethala, B.B. Panigrahi. J. Mater. Res. 34, 777 (2017). [Crossref](#)
20. V.I. Nizhenko, L.I. Floka. Surface tension of liquid metals. Moscow, Metallurgiya (1981) 208 p. (in Russian)
21. A. A. Bugaev, V. A. Lukoshkin, V. A. Urpin, D. G. Yakovlev. Tech. Phys. 58, 908 (1988). (in Russian)